THE JOURNAL OF PHYSICAL CHEMISTRY C

pubs.acs.org/JPCC

Article

UV-Laser Interference Lithography for Local Functionalization of Plasmonic Nanostructures with Responsive Hydrogel

Nestor Gisbert Quilis, Simone Hageneder, Stefan Fossati, Simone K. Auer, Priyamvada Venugopalan, Anil Bozdogan, Christian Petri, Alberto Moreno-Cencerrado, Jose Luis Toca-Herrera, Ulrich Jonas, and Jakub Dostalek*

Cite This: *J. Phys. Chem. C* 2020, 124, 3297−3305

Read Online

ACCESS | Metrics & More | Article Recommendations | Supporting Information

ABSTRACT: A novel approach to local functionalization of plasmonic hotspots at gold nanoparticles with biofunctional moieties is reported. It relies on photocrosslinking and attachment of a responsive hydrogel binding matrix by the use of a UV interference field. A thermoresponsive poly(*N*-isopropylacrylamide)-based (pNIPAAm) hydrogel with photocrosslinkable benzophenone groups and carboxylic groups for its postmodification was employed. UV-laser interference lithography with a phase mask configuration allowed for the generation of a high-contrast interference field that was used for the recording of periodic arrays of pNIPAAm-based hydrogel features with the size as small as 170 nm. These hydrogel arrays were overlaid and attached on the top of periodic arrays of gold nanoparticles, exhibiting a diameter of 130 nm and employed as a three-dimensional binding matrix in a plasmonic biosensor. Such a hybrid material was postmodified with ligand biomolecules and utilized for plasmon-enhanced fluorescence readout of an immunoassay. Additional enhancement of the fluorescence sensor signal by the collapse of the responsive hydrogel binding matrix that compacts the target analyte at the plasmonic hotspot is demonstrated.

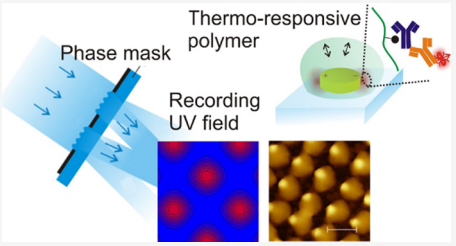

INTRODUCTION

A variety of naturally occurring or synthetic biopolymers has been tailored for specific biomedical[1] and analytical[2] applications, and among these, stimuli-responsive polymers represent particularly attractive "smart" materials capitalizing on their ability to undergo physical or chemical changes triggered by an external stimulus.[3−5] Such materials can be incorporated into architectures that are on-demand actuated by stimuli, including temperature, pH, or electric current.[6−8] A prominent example of a responsive polymer is the poly(*N*-isopropylacrylamide) (pNIPAAm), which is well-known for its thermoresponsive behavior. pNIPAAm exhibits a lower critical solution temperature (LCST) with pronounced and fully reversible hydrophobic-to-hydrophilic transition close to the body temperature.[9] pNIPAAm has been utilized in drug delivery micro/nanogels,[10] for modulating cellular interactions,[5,11] biosensors,[12] and in opto-responsive coatings.[13]

The nanoscale patterning of responsive polymer materials is important to let them serve in diverse areas ranging from sensing,[14] optical components,[15] and catalysis[16] to tissue engineering[17] and cell biology.[18] Self-assembly represents a widely used method for the preparation of nano- and microstructures based on, for instance, block-copolymer that combines hydrophobic and hydrophilic segments.[19,20] In addition, casting of microstructures by polymerization in template cavities has been utilized for the fabrication of miniature responsive polymer objects actuated in aqueous solution.[21] To prepare structures that are attached to a solid surface, photolithography has been extensively used for various types of responsive polymer structures.[22] Shadow mask photolithography-based methods typically enable facile means for the patterning of microstructures over macroscopic areas. To gain finer nanoscale control of the morphology of responsive polymer structures, electron beam lithography was employed for the structuring on a small footprint.[23,24] In addition, UV nanoimprint lithography has been introduced to harness both nanoscale precision and compatibility with scaled-up production.[25] This method is based on a transfer of a target motif carried by a stamp to a polymer layer by the subsequent polymerization[26] or photocrosslinking.[27]

Metallic nanostructures can be incorporated into responsive polymer architectures to provide means for their optical actuating[28,29] or to be employed for the optical readout in bioanalytical applications.[30] Metallic nanostructures support localized surface plasmons (LSPs) that tightly confine the electromagnetic field in their vicinity through its coupling with collective charge density oscillations. The resonant excitation of LSPs is accompanied by a strongly enhanced electromagnetic field intensity,[31] locally increased temperature[32] or, for instance, an emission of hot electrons.[33] In bioanalytical

Received: November 26, 2019
Revised: January 9, 2020
Published: January 10, 2020

https://dx.doi.org/10.1021/acs.jpcc.9b11059
J. Phys. Chem. C 2020, 124, 3297−3305

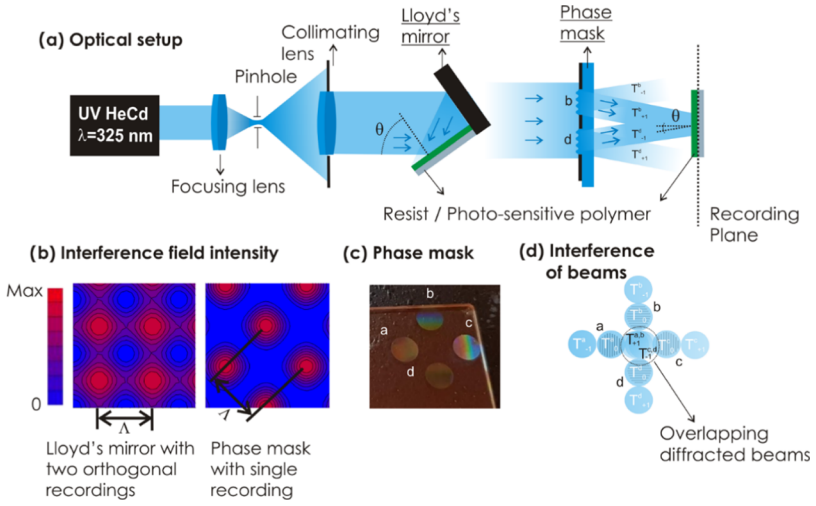

Figure 1. (a) Optical configuration of the UV-laser interference lithography with Lloyd's mirror configuration (left) and the phase mask configuration (right). (b) Simulations of the interference field generated by Lloyd's mirror configuration (left) and developed phase mask (right). (c) Schematics of the phase mask carrying four circular transmission gratings marked as a, b, c, and d. (d) Schematics of the overlapping of collimated waves at the recording plane with zero-order T_0 and first-order diffracted $T_{+/-1}$ beams.

sensing applications, the LSPs are utilized for the probing of target molecules that are brought in contact with the metallic nanoparticles. In affinity-based plasmonic biosensors, mostly thiol self-assembled monolayers are deployed at the two-dimensional (2D) surface of plasmonic nanoparticles for attaching of ligand molecules that specifically capture target molecules from the analyzed liquid sample.[34] In general, the sensitivity of LSP-based biosensors can be advanced by strategies that allow for selective capture of target analytes only at the regions where the electromagnetic field is confined (e.g., edges and walls of cylindrical gold nanoparticles), commonly referred as to "plasmonic hotspots". To deploy ligand molecules that specifically capture target species at the plasmonic hotspot, 2D surface architectures were combined with lithography-based strategies generating masks.[35,36] In addition, other strategies, including material-orthogonal chemistries,[37] surface plasmon-triggered polymerization,[38] and surface plasmon-enhanced two-photon cleavage of photosensitive organic moieties,[39] have been reported to attain local functionalization of metallic nanostructures.

The LSPs typically probe rather small subareas of the metallic nanoparticles, and their field reaches only a short distance of several tens of nanometers away from their surface.[40] Therefore, the performance of various LSP-based biosensor modalities is hindered by the reduced probability of analyte capture in these narrow spatial zones, where the electromagnetic field is confined. The use of biointerfaces composed of 3D polymer brushes or networks provides means to increase the surface area and respective binding capacity,[41,42] offering higher capture probability of the target analyte in the hotspot zones probed by LSPs. The present paper reports on the local attachment of a 3D hydrogel binding matrix in the vicinity of well-ordered gold nanoparticles, which can be postmodified for specific affinity capture of target analytes and actuated for their compacting at the plasmonic hotspot.

METHODS

Materials. OrmoPrime08, S1805 and SU-8 photoresist, SU-8 2000 thinner, and an AZ303 developer were purchased from Micro Resist Technology (Germany). Dimethyl sulfoxide (DMSO), acetic acid, propylene glycol monomethyl ether acetate, and 1-ethyl-3-(3-dimethylaminopropyl)carbodiimide (EDC) were obtained from Sigma Aldrich (Germany). pNIPAAm-based terpolymer composed of *N*-isopropylacrylamide, methacrylic acid, and 4-methacryloyloxybenzophenone (in a ratio of 94:5:1), benzophenone disulfide, and 4-sulfotetrafluorophenol (TFPS) were synthesized in our laboratory as previously reported.[43−45]

IgG from mouse serum (mIgG, I 5381), Tween 20 (P9416), and bovine serum albumin (A2153) were purchased from Sigma Aldrich (Austria). Phosphate-buffered saline (PBS) and sodium acetate were obtained from VWR Chemicals (Austria). Alexa Fluor 790 goat anti-mouse IgG (a-mIgG, A11375) was acquired from Life Technologies (Eugene, OR).

Optical Configuration of Laser Interference Lithography. A He-Cd laser (IK 3031 R-C) from Kimmon (Japan) emitting at λ = 325 nm with 4 mW was employed. The coherent beam was expanded with a spatial filter consisting of a pinhole (10 μm) and ×40 microscope lens. For Lloyd's mirror configuration, the expanded beam was collimated and impinged at a substrate carrying a photosensitive polymer and a UV-reflecting mirror with the area of several cm^2. The measured intensity of the beam in the recording plane was around 30 μW cm^{-2}. For recording with the phase mask configuration, the power of the recording field in the recording plane was increased to 400 μW cm^{-2}.

Preparation of a Phase Mask. OrmoPrime08 was employed as an adhesion promoter to prevent delamination of the resist. A Quartz substrate (20 × 20 × 1 mm) was dehydrated on a hot plate for 5 min at 200 °C, and the Ormoprime solution composed of organofunctional silanes was subsequently spun on the top at 4000 rpm for 60 s. Then, the substrate was placed on the hot plate for 5 min at 150 °C. Afterward, undiluted S1805 positive photoresist was deposited at a spin rate of 4500 rpm applied for 45 s followed by a hard-bake treatment at 100 °C for 2 min. The substrate with a photoresist was placed in Lloyd's mirror setup for recording by laser interference lithography as previously reported.[46] An interference pattern, originating from two interfering beams,

https://dx.doi.org/10.1021/acs.jpcc.9b11059
J. Phys. Chem. C 2020, 124, 3297−3305

was recorded in the photoresist layer, and a stencil mask with two symmetric circular apertures was utilized to define the area to be exposed. Custom-made stainless stencil masks were fabricated from PIU-PRINTEX (Austria) and carefully placed on top of the photoresist-coated glass substrates. The irradiation dose of 18 mJ cm^{-2} was used for the recording of two circular gratings, and subsequently, the substrate was rotated 90° and exposed once more to the same interference field with the same dose. Finally, the phase mask carrying 4 transmission gratings with two perpendicular orientations was obtained by immersing the substrate in the AZ303 developer solution diluted with deionized water (1:15 ratio) for 40 s. The angle of the collimated interfering beams was set to $\theta = 13.6°$, yielding a period of the four gratings of $\Lambda_{PM} = 690$ nm. The circular patterned area of each of the four gratings exhibited a diameter of 4 mm (see Figure 1). The measured depth of the resist gratings was about 250 nm (see Figure S1). This depth was achieved by optimizing the developing time after the recording step, and it corresponds to that providing the maximum efficiency of the first-order diffraction in transmission mode (of about 30%, data not shown).

Preparation of Gold Nanoparticles. Gold nanoparticle arrays were prepared as previously reported by the use of two-beam laser interference lithography with Lloyd's configuration.[46] Briefly, 2 nm Cr and 50 nm Au were evaporated (HHV AUTO 306 from HHV Ltd) on top of BK7 glass slides with the size of 20 × 20 mm. Subsequently, a 100 nm thick layer of S1805 positive photoresist (diluted 1:2 with propylene glycol monomethyl ether acetate) was deposited at a spin rate of 4500 rpm applied for 45 s. Hard-baking of the resist was conducted at 100 °C for 2 min. The angle between the interfering beams was set to $\theta = 20.69°$ yielding a period of $\Lambda_G = 460$ nm, and the dose was set to 6.75 mJ cm^{-2}. The parameters were adjusted to obtain arrays of cylindrical resist features with a diameter of $D = 132 \pm 5$ nm after the development step using the AZ303 developer (1:15 ratio deionized water). The arrays of resist features were transferred to the underlying gold layer using a dry etching process consisting of the bombardment of the surface with argon ions (Roth & Rau IonSys 500). Resist-free gold nanoparticles were finally obtained by exposing the substrate to an oxygen plasma process.

Preparation of Hydrogel Nanostructures. Covalent attachment of the pNIPAAm-based polymer to a BK7 glass substrate was achieved using a thin SU-8 linker layer. SU-8 was dissolved with its thinner (2% solution) and spun onto the surface of the BK7 glass substrate at the spin rate of 5000 rpm for 60 s. Afterward, the coated substrate was thermally cured in an oven at 50 °C for 2 h. To attach the pNIPAAm-based polymer to gold nanoparticles, their gold surface was modified with UV-reactive benzophenone moieties by reacting overnight with 1 mM benzophenone disulfide dissolved in DMSO. Subsequently, a 2% pNIPAAm-based polymer dissolved in ethanol was spun (2000 rpm for 2 min) over the flat substrate (with SU-8 or with gold nanoparticle arrays carrying benzophenone disulfide), followed by its overnight drying in a vacuum oven ($T = 50$ °C). The pNIPAAm-coated substrate was placed in the laser interference lithography setup. The 4-beam phase mask with $\Lambda_{PM} = 690$ nm and the pNIPAAm-based polymer-coated substrate were made parallel to each other and separated by a distance of 5.6 mm by in-house made dedicated holders. The recording was carried out by four interfering beams transmitted through the phase mask (T_{-1} and T_{+1} transmission diffraction orders) with the middle part blocked to prevent the interference with a normally propagating beam (T_0). The irradiation dose was set between 84 and 240 mJ cm^{-2} for the SU-8 substrates by adjusting the irradiation time and by keeping the intensity of the UV beam fixed (400 μW cm^{-2}). Local crosslinking of the pNIPAAm-based polymer on top of gold nanoparticle arrays was attained by exposure to the UV interference field with a dose of 108 mJ cm^{-2} and the same UV beam intensity (400 μW cm^{-2}). The irradiation dose was obtained as a product of the power of the collimated UV beam and the irradiation time that was set between 210 and 600 s. The pNIPAAm-based polymer in the nonexposed regions was washed away with deionized water, and the obtained structure was dried on the hot plate at a temperature above the LCST of pNIPAAm. For the control experiment, a 30 nm thick pNIPAAm hydrogel layer was attached and crosslinked on a flat 100 nm Au film that was reacted with benzophenone disulfide using a UV lamp (365 nm) and an irradiation dose of 2 J cm^{-2}.

Morphological Characterization. Atomic force microscopy (AFM) measurements of the patterned structures in contact with air were performed in tapping mode with the PicoPlus instrument (Molecular Imaging, Agilent Technologies). The topography in contact with water was observed in situ with the Nanowizard III (JPK Instruments, Germany) using a temperature-controlled module consisting of a flow cell with a Peltier element. Silicon nitride cantilevers DNP-S10 (Bruker) with a nominal spring constant of 0.24 N m^{-1} were utilized. Height, diameter, and lateral spacing of the nanoscale features were determined by employing Gwyddion free software.

LSPR Transmission Measurements. The polychromatic light beam emitted from a halogen lamp (LSH102 LOT-Oriel, Germany) was coupled to a multimode optical fiber. This beam was out-coupled from the fiber, collimated with a lens, and made normally incident at a substrate carrying arrays of gold nanoparticles. The transmitted beam was collected by a lens to another multimode optical fiber and delivered to a Shamrock SR-303I-B spectrometer from Andor Technology (Ireland). The obtained transmission spectra were normalized with that obtained without the investigated substrate. A flow cell with a Peltier element[12] was clamped against the substrate with the gold nanoparticles to control the temperature of the liquid flowed over its surface. Deionized water was flowed through using a peristaltic pump from Ismatec (Switzerland).

Plasmon-Enhanced Fluorescence Instrument. Fluorescence experiments were conducted with an in-house-developed fluorescence reader utilizing epifluorescence geometry.[47] The biochip carrying arrays of gold nanoparticles wrapped by the pNIPAAm-based hydrogel was placed in a microfluidic module with a flow cell and illuminated with a collimated beam at a wavelength of 785 nm and an intensity of 1.2 mW cm^{-2}. The spatial distribution of intensity of fluorescence light emitted at a wavelength of 810 nm at the biochip surface was collected and then detected with a cooled CCD camera. The optical system can be seen in Figure S2. It consisted of a diode laser (IBeam Smart 785 nm, TOptica, DE) that emitted a collimated monochromatic beam, which passed through a narrow bandwidth laser clean-up filter (LL01-785, Semrock) and a spatial filter built from a 60× microscope objective, a 40 μm pinhole, and a collimating lens (AC-254-40-B, Thorlabs) to reduce the speckles. The excitation beam traveled through a lens (AC-254-35-B, Thorlabs) and was

https://dx.doi.org/10.1021/acs.jpcc.9b11059
J. Phys. Chem. C 2020, 124, 3297−3305

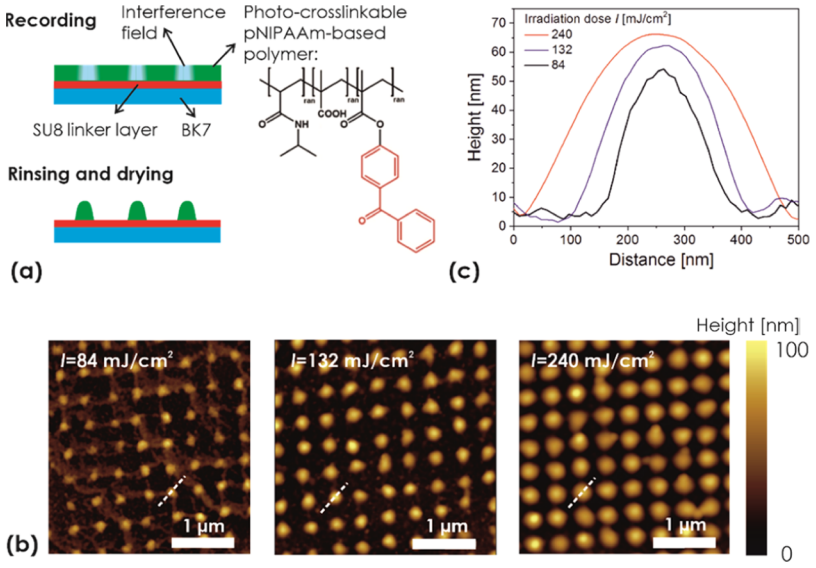

Figure 2. (a) Schematics of the local crosslinking of a responsive pNIPAAm-based polymer layer with arrays of interference maxima. The effect of the irradiation dose on (b) overall topography as observed with AFM and (c) the polymer feature cross-section.

reflected at a dichroic mirror (Di02-R785, Semrock) toward the biochip with arrays of gold nanoparticles. The incident excitation beam was then passed through another lens (AC-254-35-B, Thorlabs) to become recollimated before impinging on the biochip. The biochip was placed in the focal plane of the last lens in an in-house built microfluidic device. It was clamped against a flow cell that was temperature-controlled by the use of a Peltier device. Fluorescence light emitted at the biochip surface at a wavelength of 810 nm was collected by the same lens and passed through the dichroic mirror toward the detector. After passing an imaging lens (AC-254-80-B, Thorlabs), the remaining light at the excitation wavelength of 785 nm was blocked with a notch filter (NF03-785E-25, Semrock) and a fluorescence bandpass filter (FF01-810/10-25, Semrock) before hitting a scientific EM-CCD camera (Ixon 885K, Andor, UK). The camera was operated at a stable temperature of −70 °C, and 10 images for 1 s exposure time were accumulated for an increased dynamic range. The whole device was controlled, and the data were collected by the in-house developed dedicated LabView-based software. It was used for the acquisition of fluorescence intensity from arrays of circular spots (each spot exhibited a diameter of 220 μm). The acquired fluorescence intensity from each spot was averaged over its area from the raw image acquired by the optical system with an optical resolution limited to about 4 μm owing to the size of the CCD camera pixel of 8 μm and optical magnification of 2.

Immunoassay Experiment. COOH groups carried by the pNIPAAm-based polymer chains on the biochip surface were activated by reacting for 15 min with EDC and TFPS dissolved in water at a concentration of 75 and 21 mg/mL, respectively. A substrate with pNIPAAm-based polymer networks forming a hydrogel nanostructure overlaid with gold nanoparticle arrays or a thin hydrogel layer on the top of a flat gold film was then rinsed with deionized water, dried, and reacted with mIgG dissolved at a concentration of 50 μg/mL in acetate buffer (pH 4) for 90 min under shaking. Afterward, the surface was washed two times for 15 min with PBS working buffer, which contained 0.05% Tween 20 and 1 mg/mL BSA. Then, the substrate was rinsed, dried, and clamped into a flow cell to perform plasmon-enhanced fluorescence observation of affinity binding inside the pNIPAAm-based hydrogel matrix. The flow cell was connected to a peristaltic pump through a microfluidic tubing system with a total volume of ≈1 mL. After establishing a stable baseline in the fluorescence signal upon a flow of working buffer (PBS with Tween and BSA), changes in the fluorescence signal emitted from different spots on the biochip due to the affinity binding were measured using dedicated LabView-based software. A dilution series of a-mIgG (conjugated with Alexa Fluor 790) at concentrations of 1, 5, 10, 50, and 100 pM and a volume of 1 mL were flowed over the biochip surface for 15 min, followed by a 5 min rinsing with the working buffer in between.

RESULTS AND DISCUSSION

At first, the patterning of pNIPAAm-based nanostructures by UV-laser interference lithography (UV-LIL) with a phase mask configuration is described. This approach allows for generating a high-contrast UV interference field pattern that is used for nanoscale control of the attachment and crosslinking of a responsive pNIPAAm-based polymer. This strategy is then employed to overlay at the nanoscale pNIPAAm structure with periodic arrays of gold nanoparticles supporting LSPs. The LSPs supported by these nanoparticles are employed to observe swelling and collapsing of the pNIPAAm hydrogel, which caps the gold nanoparticle surface, by means of detuning the resonant wavelength at which the LSPs are optically excited. In addition, this wavelength is closely tuned to the absorption and emission wavelengths of a fluorophore that serves as a label in fluorescence immunoassays. Consequently, the pNIPAAm-based hydrogel is employed as a binding matrix that is postmodified with a protein ligand and utilized for surface plasmon-amplified fluorescence readout of the assay. Additional signal enhancement by the collapse of the gel is demonstrated using the developed hybrid plasmonic material.

UV-Laser Interference Lithography with a Phase Mask. As illustrated in Figure 1a, laser interference lithography relies on the recording of an interference pattern formed by overlapping coherent optical beams to a photosensitive polymer layer. In the UV-LIL configuration with Lloyd's

https://dx.doi.org/10.1021/acs.jpcc.9b11059
J. Phys. Chem. C 2020, 124, 3297−3305

mirror shown in Figure 1b, a periodic sinusoidal pattern is recorded by two plane waves impinging on a layer of the photosensitive polymer at an angle θ. The recorded structure typically exhibits smoothly varying features[48] arranged in an array with a period equal to $\Lambda = \lambda/2\sin(\theta)$, where λ is the wavelength of the recording interference beam. To record a periodic pattern with higher contrast, we employed four interfering waves with a setup shown in Figure 1a, featuring a phase mask. This phase mask consists of four transmission gratings a, b, c, and d on a UV-transparent glass slide, as depicted in Figure 1c. The area between the gratings is made reflective; thus, only the coherent plane wave impinging on the grating regions of the mask is transmitted. Each grating diffracts the coherent incident beam to a series of transmission orders marked as T_{-1}, T_0, and T_{+1}, as shown in Figure 1d. These orders propagate to different directions, and the mask was designed so that four coherent diffractive beams T_{-1} and T_{+1} overlap in the central zone at a distance of 5.6 mm, forming an interference field as indicated in Figure 1c. This pattern exhibits arrays of more confined peaks in the harmonic spatial distribution of the interference field intensity when compared to that achieved by the conventional Lloyd's mirror configuration with two interfering beams, see Figure 1b. The intensity of the pattern generated by four interfering beams (phase mask configuration) drops to zero between the peaks, while that for the sequential orthogonal recording of two interfering beams (Lloyd's mirror configuration) does not. The period of the pattern generated by the four coherent interfering beams is $\Lambda = \Lambda_{PM}/\sqrt{2}$, where Λ_{PM} is the period of the transmission gratings on the phase mask. The full width of the half maximum (FWHM) of the peaks in this pattern is of $\Lambda/2$. To observe the interference pattern formed by the phase mask with a grating period of Λ_{PM} = 690 nm at a wavelength of λ = 325 nm, it was recorded to a layer of S1805 positive-tone photoresist with a thickness of 100 nm. After developing the recorded field distribution (an irradiation dose of 27 mJ cm^{-2}), atomic force microscopy (AFM) was employed for the observation of the structured resist topography. The obtained results presented in Figure S1 show a series of circular holes in the resist layer with a periodicity of Λ = 490 ± 4 nm, which is in agreement with the simulated profile of the interference field distribution, as shown in Figure 1b.

Recording of pNIPAAm-Based Hydrogel Arrays. To prepare arrays of responsive pNIPAAm-based hydrogel features, the terpolymer shown in Figure 2a was used. This terpolymer carries pendant benzophenone groups for photocrosslinking and covalent attachment to a solid surface upon irradiation with UV light.[43] In addition, methacrylic acid was copolymerized, as the incorporated carboxyl groups promote swelling in water and provide a chemical postmodification site for the incorporation of biomolecules via amine coupling.[49]

The pNIPAAm-based polymer layer with a thickness of 70 nm was spun onto a glass substrate carrying a thin adhesion-promoting SU-8 film. After complete drying of the pNIPAAm polymer layer, the substrate was placed in the 4-beam UV-LIL optical system and exposed to the interference pattern generated by a phase mask to record a crosslinked structure with a period of Λ_H = 488 nm. Upon irradiation, the pNIPAAm-based polymer in the area of high UV intensities is crosslinked and attached to the substrate, while the unexposed areas remain unchanged. Therefore, after subsequent rinsing of the layer with ethanol and water, the crosslinked pNIPAAm network remains in the exposed zones and only noncrosslinked polymer is washed away in the area in between. After drying on a hot plate at temperature T = 100 °C, AFM images of the pNIPAAm surface topography were acquired. In Figure 2b, a periodic pattern of nonconnected domains of crosslinked pNIPAAm with a height similar to the initial thickness of the original polymer layer can be seen. When increasing the irradiation dose of the UV light from I = 84 to 132 and 240 mJ cm^{-2}, the pNIPAAm domains exhibit an increasing diameter (FWHM) of D = 168 ± 9, 208 ± 8, and 293 ± 9 nm, respectively, which were determined from the cross-sections presented in Figure 2c. These values are around FWHM of the peaks in the interference field pattern of $\Lambda_H/2$ = 244 nm, and the changes in D reflect the nonlinear dependence of the crosslinking on the irradiation dose. In addition, the height of the structure between 50 and 65 nm determined from the cross-sections in Figure 2c are lower than the thickness of the original (noncrosslinked) pNIPAAm film, which can be ascribed to the effect of smearing of the recorded features after their swelling and drying before the AFM observation.

Interestingly, the topography of the pNIPAAm-based domains changes depending on the conditions in which they are dried prior to the AFM observation in air. As Figure 3 illustrates, the height of the features strongly decreases, and the diameter increases when the surface is rinsed with water and dried at room temperature. This observation relates to what is already reported for sinusoidal corrugation of similar pNIPAAm crosslinked layers[48] and nanoimprinted nanopillars.[27] It can be attributed to the strong deformation of the elastic polymer network by the surface tension of the aqueous medium upon evaporation. The elasticity of the wet pNIPAAm network is strongly temperature-dependent due to its thermoresponsive solvation properties: below the LCST of 32 °C, the network swells in water and forms a soft structure that is planarized in the drying process (the height decreases by a factor of about 10). However, above the LCST in water, the polymer network collapses and forms more compact, rigid domains that are resistant to mechanical deformation upon drying. This swelling behavior was also investigated by acquiring AFM images of the prepared thermoresponsive nanostructures in water at varying temperatures around the LCST. As shown in Figure 4, at T = 30 °C, the topography of the swollen soft pNIPAAm structure is barely captured by the AFM tip. However, when the temperature is increased above

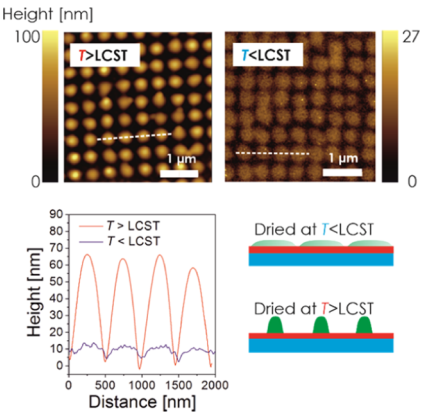

Figure 3. AFM observation of nanostructured pNIPAAm hydrogel topography dried at a temperature below and above the LCST. The structure was prepared with an irradiation dose of 240 mJ/cm^2.

https://dx.doi.org/10.1021/acs.jpcc.9b11059
J. Phys. Chem. C 2020, 124, 3297−3305

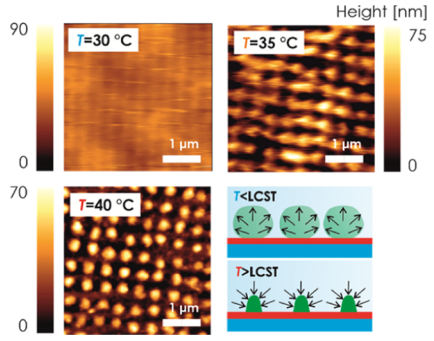

Figure 4. AFM observation of nanostructured pNIPAAm hydrogel topology in water for the temperature T = 30, 35, and 40 °C. The structure was prepared with an irradiation dose of 240 mJ/cm^2.

the LCST to T = 35 °C, the inscribed pattern becomes apparent for the collapsed and more rigid hydrogel network. Interestingly, upon further temperature increase to T = 40 °C, the observed geometry in water fully resembles the morphology that was recorded in air, as presented in Figure 2b.

Hybrid Au-pNIPAAm Nanostructures. The developed approach for the preparation of arrays with thermoresponsive pNIPAAm-based features was further applied to gold nanoparticle arrays to yield a hybrid plasmonic nanomaterial. First, gold nanoparticle arrays were prepared on a glass surface using UV-LIL with Lloyd's mirror configuration and a dry etching protocol, as previously reported.[46] The obtained cylindrical gold nanoparticle exhibited a diameter of D = 132 ± 5 nm, a height of about 50 nm, and an array periodicity of Λ_G = 463 ± 2 nm, as revealed by the AFM image in Figure 5a. Afterward, the gold surface of the nanoparticles was modified with a self-assembled monolayer (SAM) of benzophenone disulfide, on top of which a pNIPAAm polymer film was deposited (the benzophenone disulfide serves here as a linker for the covalent photoattachment of the polymer chains to gold[44]).

Then, the same phase mask-based procedure (for recording the four-beam UV interference field with the period of Λ_H = 488 ± 2 nm) was applied to generate arrays of pNIPAAm-based polymer structures, followed by rinsing with water and drying.

To circumvent the difficulty to precisely align both arrays of the hydrogel features and the gold nanoparticles, a slight mismatch of the array periodicities by 5% was intentionally applied to yield a Moiré effect between both features. As a result, it is expected that the topography will vary periodically across the surface, resulting in a repeating pattern of areas with aligned and with misaligned geometry. The characteristic size of these domains can be estimated as $\Lambda_H \cdot \Lambda_G/(\Lambda_H - \Lambda_G)$ in the range of about 8 μm. Figure 5b shows an AFM image for the topography of a 2 × 2 μm subarea of the structure that exhibits hydrogel features aligned with the gold nanoparticle arrays after drying below the LCST. Apparently, the gold nanoparticles are visible as areas with an increased height of about 85 nm surrounded by partially planarized pNIPAAm zones of lower height that spread to a diameter of about 400 nm (see also the representative cross-section in Figure S3). When the structure is exposed to water and dried again above the LCST, the morphology changes, as shown in Figure 5c. The metallic nanoparticle topography is not protruding through the pNIPAAm hydrogel, which appears more compacted and spreading to a smaller diameter of about 300 nm. The maximum height of the pNIPAAm features (with metallic nanoparticle inside) of 90 nm is slightly higher than for the structure dried below LCST. The morphology variations due to drying in the swollen and collapsed state of pNIPAAm networks attached to gold nanoparticles are less pronounced than on the flat SU-8 film. It can be attributed to different means of the attachment (swelling and collapsing on the curved surface of Au nanoparticle walls) and to the potential difference in the interaction of pNIPAAm chains with SU-8 and BK7 glass (surrounding the hydrogel structure). For comparison, an area where the gold nanoparticles and hydrogel features are misaligned is presented in Figure 5d. The patterned hydrogel features around the metallic structures exhibit more irregular morphology compared to those measured without the gold nanoparticles in Figures 2–4. This observation can be attributed to gradually changing alignment between the center of the hydrogel feature and the gold nanoparticle along the surface and the fact that the collapse tends to pull pNIPAAm-based polymer toward gold where the attachment is utilized via the benzophenone disulfide linker.

Actuating of LSP. The collapse of the pNIPAAm hydrogel is associated with an increase of the polymer volume fraction and the refractive index on the surface of gold nanoparticles. Therefore, the pNIPAAm collapse around these metallic objects detunes the localized surface plasmon resonance

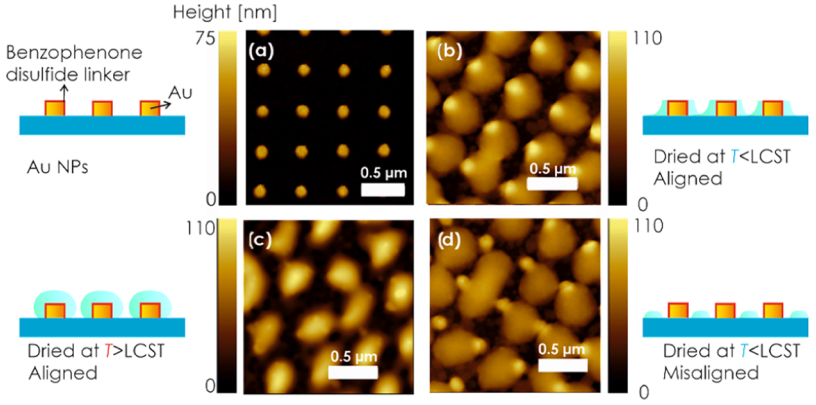

Figure 5. AFM topography of (a) gold nanoparticle arrays subsequently covered with covalently attached pNIPAAm-based nanostructures that are aligned with the gold nanoparticles and dried (b) below and (c) above the LCST. (d) Example of misaligned arrays of gold nanoparticles with pNIPAAm-based nanostructures dried below the LCST.

https://dx.doi.org/10.1021/acs.jpcc.9b11059
J. Phys. Chem. C 2020, 124, 3297–3305

(LSPR) and manifests itself as a redshift of the resonant wavelength. Figure 6a shows the transmission spectra

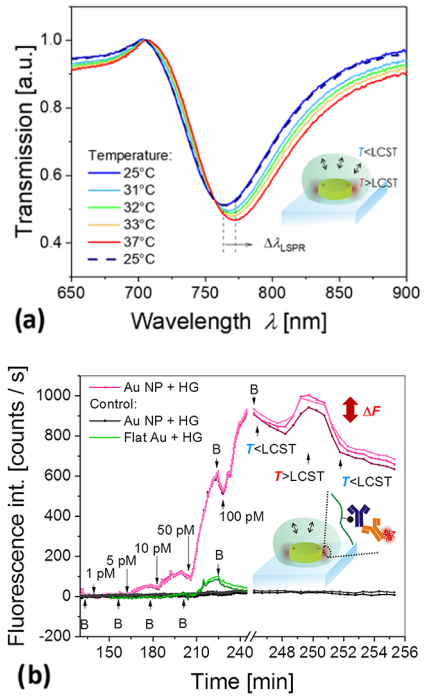

Figure 6. (a) Measured reversible shift in LSPR spectra upon temperature-induced swelling and collapse of the pNIPAAm-based hydrogel wrapped over metallic nanoparticles. (b) Employment of the hybrid material for plasmonic amplification of a fluorescence immunoassay with the pNIPAAm-based hydrogel serving as an affinity binding matrix that can be swollen and collapsed by an external temperature stimulus. The red-colored lines show the fluorescence signal acquired from spots with a diameter of 220 μm at different locations on the same biochip carrying the pNIPAAm-based hydrogel that was functionalized with ligands. The black curves correspond to control spots on the same biochip that were not functionalized with the ligand molecules, and the green curves show the control experiment on a planar-functionalized hydrogel binding matrix attached to the flat gold film. The analyte concentration is clearly indicated in the graph, and B corresponds to the rinsing step with working buffer.

measured over the area of about 1 mm^2, which averages the variations in the alignment between gold nanoparticles and hydrogel features with a domain size <10 μm. LSPR for the structure at the temperature T = 25 °C manifests itself as a dip in the transmission spectrum centered at a wavelength of λ_{LSPR} = 763.9 nm. The gradual collapse of the hydrogel induces a red-shift of the LSPR wavelength upon an increase in the temperature. At a temperature of T = 37 °C, far above the LCST, the LSPR wavelength shifts to 771.9 nm. These changes are fully reversible, as after cooling to T = 25 °C, the LSPR spectrum shifts back to the original shape. It is worth noting that the observed shift of about 6 nm is half of that measured for a structure covered with a compact pNIPAAm hydrogel film (data not shown), which can be ascribed to the fact that about half of the nanoparticles is not in contact with the polymer due to the periodic regions of misalignment in the Moiré pattern.

LSP-Enhanced Fluorescence Assay. Finally, the developed structure was tested to serve as a biochip interface for the fluorescence readout of an immunoassay. First, the responsive pNIPAAm-based hydrogel features wrapping (about half) of the gold nanoparticles that were postmodified with mouse IgG antibodies (mIgG). The polymer carboxylic groups were employed for establishing covalent bonds between the lysine groups of the protein and the polymer chain based on the established amine coupling scheme.[49] Then, the substrate was clamped against a flow cell, and a series of liquid samples with an increasing concentration of goat antibodies specific to mIgG (a-mIgG) were pumped over its surface. To detect the affinity binding, the goat antibody a-mIgG was labeled with an organic dye (Alexa Fluor 790). This label exhibits its absorption and emission wavelengths (λ_{ex} = 785 nm, λ_{em} = 810 nm) in the vicinity of the LSPR wavelength (λ_{LSPR} = 764 nm). Therefore, the kinetics of the affinity binding of a-mIgG from the liquid sample was measured using plasmon-enhanced fluorescence.[50] The surface of the sample was irradiated by a laser beam at a wavelength of 785 nm that resonantly couples to LSPs and locally excites the bound fluorophores with its enhanced field intensity. The emitted light at a wavelength of 810 nm was collected with a home built instrument[47] separated from the excitation beam using a dichroic mirror, bandpass filter, and notch filter and detected with a cooled CCD camera. The fluorescence signal was acquired with dedicated software from a series of spots carrying the gold nanoparticle arrays in reference to an area without nanoparticles, and the data were tracked in time upon sequential flow of analyte samples. The fluorescence intensity was averaged over the surface of each circular spot with a diameter of 220 μm that was much larger than the size of domains with aligned and misaligned arrays of gold nanoparticles and hydrogel features. The liquid samples were prepared from phosphate-buffered saline that was spiked with a-mIgG at concentrations of 1, 5, 10, 50, and 100 pM. Each sample was flushed over the surface for 15 min, followed by 5 min rinsing. As Figure 6b shows, the binding of a-mIgG manifests itself as a gradual increase in the fluorescence signal, and upon rinsing, a fluorescence intensity decrease occurs due to bleaching of the emitters. The fluorescence signal on gold nanoparticle arrays capped with the pNIPAAm hydrogel matrix (red curves in Figure 6a) is about 6 times higher compared to a control experiment (green curves in 6a). The control experiment was carried out on the hydrogel biointerface prepared in the form of a layer attached to a flat nonstructured gold film. It is worth noting that the plasmonic enhancement on the structured surface is probably higher than the factor of 6 due to the fact that the control flat architecture exhibits a larger area for the capture of the target analyte and that at least half of the metallic nanoparticles are not capped with the hydrogel binding matrix due to the miss-alignment. The measured data for a structured hydrogel biointerface overlaid with gold nanoparticles indicate that the limit of detection of the prepared biochip is 0.7 pM (determined for the standard deviation fluorescence signal baseline of 2 counts/s and the slope of the fluorescence signal of 9 counts/s/pM). After this titration experiment, the temperature of the biochip surface was increased from 25 to 40 °C, above the LCST of the hydrogel. As seen in Figure 6b, the induced collapse of the responsive hydrogel with the affinity-captured and fluorophore-labeled a-mIgG leads to an increase of the fluorescence signal by about 20%. This is due to the collapse and compacting of the hydrogel, which increases the polymer volume fraction and affinity-bound analyte molecules closer to the gold surface, where the plasmonic hotspot is located. This observation corroborates that affinity binding occurs in the

https://dx.doi.org/10.1021/acs.jpcc.9b11059
J. Phys. Chem. C 2020, 124, 3297−3305

vicinity of the metallic nanoparticles within the matrix of the responsive pNIPAAm-based polymer network and indicates that the triggered collapse can provide an additional enhancement mechanism for high sensitivity fluorescence assays.

CONCLUSIONS

A technique based on four-beam laser interference lithography utilizing a phase mask-based configuration allows for the preparation of well-defined responsive hydrogel nanostructures with the tailored spacing and diameter. Periodic arrays of pNIPAAm-based hydrogel nanostructures exhibiting a disk shape with a tunable diameter, as low as 170 nm, were prepared with a submicron period. The temperature-induced swelling and collapse of the inscribed polymer features were investigated, and their local attachment on top of the periodic gold nanoparticle arrays was achieved based on the Moiré effect. The fully reversible actuation by temperature changes was demonstrated by measuring the variations in LSPR of the gold nanoparticle arrays. In addition, the pNIPAAm-based hydrogel was postmodified with biorecognition elements to serve as a 3D high binding capacity matrix, and a model bioassay based on fluorescence readout was conducted. The limit of detection was proven to be in the sub-picomolar range owing to the plasmonic amplification of the fluorescence signal by the plasmonic nanoparticles. Finally, the capability of the pNIPAAm network to compact the affinity-captured analyte at the plasmonic hotspots by a temperature-induced polymer collapse was tested. The presented hybrid architecture provides a novel approach for the local attachment of chemical and biological species in the vicinity of metallic nanostructures to fully exploit the probing with the LSP field at the so-called plasmonic hotspots, where the optical field intensity is the strongest.

ASSOCIATED CONTENT

Supporting Information

The Supporting Information is available free of charge at https://pubs.acs.org/doi/10.1021/acs.jpcc.9b11059.

> Schematic and atomic force spectroscopy images of the phase mask and recorded interference pattern employing a positive photoresist; schematic of the optical setup used for the plasmon-enhanced spectroscopy assay; cross-sections of AFM topography of hydrogel nanostructures (PDF)

AUTHOR INFORMATION

Authors

Nestor Gisbert Quilis − *BioSensor Technologies, AIT-Austrian Institute of Technology GmbH, 3430 Tulln, Austria*

Simone Hageneder − *BioSensor Technologies, AIT-Austrian Institute of Technology GmbH, 3430 Tulln, Austria*

Stefan Fossati − *BioSensor Technologies, AIT-Austrian Institute of Technology GmbH, 3430 Tulln, Austria*

Simone K. Auer − *BioSensor Technologies, AIT-Austrian Institute of Technology GmbH, 3430 Tulln, Austria*

Priyamvada Venugopalan − *BioSensor Technologies, AIT-Austrian Institute of Technology GmbH, 3430 Tulln, Austria; CEST Kompetenzzentrum für elektrochemische Oberflächentechnologie GmbH, TFZ, Wiener Neustadt, 2700 Wiener Neustadt, Austria*

Anil Bozdogan − *CEST Kompetenzzentrum für elektrochemische Oberflächentechnologie GmbH, TFZ, Wiener Neustadt, 2700 Wiener Neustadt, Austria*

Christian Petri − *Macromolecular Chemistry, Department Chemistry-Biology, University of Siegen, Siegen 57076, Germany*

Alberto Moreno-Cencerrado − *Institute for Biophysics, Department of Nanobiotechnology, University of Natural Resources and Life Sciences Vienna (BOKU), Vienna 1190, Austria*

Jose Luis Toca-Herrera − *Institute for Biophysics, Department of Nanobiotechnology, University of Natural Resources and Life Sciences Vienna (BOKU), Vienna 1190, Austria*

Ulrich Jonas − *Macromolecular Chemistry, Department Chemistry-Biology, University of Siegen, Siegen 57076, Germany;* orcid.org/0000-0002-2161-4541

Jakub Dostalek − *BioSensor Technologies, AIT-Austrian Institute of Technology GmbH, 3430 Tulln, Austria;* orcid.org/0000-0002-0431-2170

Complete contact information is available at: https://pubs.acs.org/10.1021/acs.jpcc.9b11059

Notes

The authors declare no competing financial interest.

ACKNOWLEDGMENTS

N.G.Q. acknowledges funding from the European Union's Horizon 2020 research and innovation program under Grant agreement no. 642787, Marie Sklodowska-Curie Innovative Training Network BIOGEL. P.V. was supported by the project jointly funded by Agence Nationale de la Recherche (ANR) and the Austrian Science Fund (FWF) under the grant agreements ANR-15-CE29-0026 and I 2647, respectively. S.H., S.F., C.P., and J.D. received support from the European Union's Horizon 2020 research and the innovation program under Grant Agreement no. 633937, project ULTRAPLACAD. S.A. is grateful for the support from FEMTEC and S.H., S.F., and J.D. were supported by the Austrian Research Promotion Agency (FFG) with Grant agreement no. 861578 (ERANET project PLABAN).

REFERENCES

(1) Green, J. J.; Elisseeff, J. H. Mimicking Biological Functionality with Polymers for Biomedical Applications. *Nature* **2016**, *540*, 386.

(2) Mateescu, A.; Wang, Y.; Dostalek, J.; Jonas, U. Thin Hydrogel Films for Optical Biosensor Applications. *Membranes* **2012**, *2*, 40−69.

(3) Liu, F.; Urban, M. W. Recent Advances and Challenges in Designing Stimuli-Responsive Polymers. *Prog. Polym. Sci.* **2010**, *35*, 3−23.

(4) Wei, M.; Gao, Y.; Li, X.; Serpe, M. J. Stimuli-Responsive Polymers and Their Applications. *Polym. Chem.* **2017**, *8*, 127−143.

(5) De las Heras Alarcón, C.; Pennadam, S.; Alexander, C. Stimuli Responsive Polymers for Biomedical Applications. *Chem. Soc. Rev.* **2005**, *34*, 276−285.

(6) Jiang, N.; Zhuo, X.; Wang, J. Active Plasmonics: Principles, Structures, and Applications. *Chem. Rev.* **2017**, *118*, 3054−3099.

(7) Huck, W. T. Responsive Polymers for Nanoscale Actuation. *Mater. Today* **2008**, *11*, 24−32.

(8) Sidorenko, A.; Krupenkin, T.; Taylor, A.; Fratzl, P.; Aizenberg, J. Reversible Switching of Hydrogel-Actuated Nanostructures into Complex Micropatterns. *Science* **2007**, *315*, 487−490.

(9) Haq, M. A.; Su, Y.; Wang, D. Mechanical Properties of Pnipam Based Hydrogels: A Review. *Mater. Sci. Eng., C* **2017**, *70*, 842−855.

(10) Guan, Y.; Zhang, Y. Pnipam Microgels for Biomedical Applications: From Dispersed Particles to 3d Assemblies. *Soft Matter* **2011**, *7*, 6375−6384.
(11) Nash, M. E.; Healy, D.; Carroll, W. M.; Elvira, C.; Rochev, Y. A. Cell and Cell Sheet Recovery from Pnipam Coatings; Motivation and History to Present Day Approaches. *J. Mater. Chem.* **2012**, *22*, 19376−19389.
(12) Toma, M.; Jonas, U.; Mateescu, A.; Knoll, W.; Dostalek, J. Active Control of Spr by Thermoresponsive Hydrogels for Biosensor Applications. *J. Phys. Chem. C* **2013**, *117*, 11705−11712.
(13) Kawano, T.; Niidome, Y.; Mori, T.; Katayama, Y.; Niidome, T. Pnipam Gel-Coated Gold Nanorods for Targeted Delivery Responding to a near-Infrared Laser. *Bioconjugate Chem.* **2009**, *20*, 209−212.
(14) Erickson, D.; Mandal, S.; Yang, A. H.; Cordovez, B. Nanobiosensors: Optofluidic, Electrical and Mechanical Approaches to Biomolecular Detection at the Nanoscale. *Microfluid. Nanofluid.* **2008**, *4*, 33−52.
(15) Paquet, C.; Kumacheva, E. Nanostructured Polymers for Photonics. *Mater. Today* **2008**, *11*, 48−56.
(16) Ghosh, S.; Kouamé, N. A.; Ramos, L.; Remita, S.; Dazzi, A.; Deniset-Besseau, A.; Beaunier, P.; Goubard, F.; Aubert, P.-H.; Remita, H. Conducting Polymer Nanostructures for Photocatalysis under Visible Light. *Nat. Mater.* **2015**, *14*, 505.
(17) Slepicka, P.; Kasalkova, N. S.; Siegel, J.; Kolska, Z.; Bacakova, L.; Svorcik, V. Nano-Structured and Functionalized Surfaces for Cytocompatibility Improvement and Bactericidal Action. *Biotechnol. Adv.* **2015**, *33*, 1120−1129.
(18) Nie, Z.; Kumacheva, E. Patterning Surfaces with Functional Polymers. *Nat. Mater.* **2008**, *7*, 277.
(19) Cheng, J. Y.; Mayes, A. M.; Ross, C. A. Nanostructure Engineering by Templated Self-Assembly of Block Copolymers. *Nat. Mater.* **2004**, *3*, 823.
(20) Hu, H.; Gopinadhan, M.; Osuji, C. O. Directed Self-Assembly of Block Copolymers: A Tutorial Review of Strategies for Enabling Nanotechnology with Soft Matter. *Soft Matter* **2014**, *10*, 3867−3889.
(21) Zhang, H.; Mourran, A.; Möller, M. Dynamic Switching of Helical Microgel Ribbons. *Nano Lett.* **2017**, *17*, 2010−2014.
(22) Chen, J.-K.; Chang, C.-J. Fabrications and Applications of Stimulus-Responsive Polymer Films and Patterns on Surfaces: A Review. *Materials* **2014**, *7*, 805−875.
(23) Yu, Q.; Ista, L. K.; Gu, R.; Zauscher, S.; López, G. P. Nanopatterned Polymer Brushes: Conformation, Fabrication and Applications. *Nanoscale* **2016**, *8*, 680−700.
(24) Idota, N.; Tsukahara, T.; Sato, K.; Okano, T.; Kitamori, T. The Use of Electron Beam Lithographic Graft-Polymerization on Thermoresponsive Polymers for Regulating the Directionality of Cell Attachment and Detachment. *Biomaterials* **2009**, *30*, 2095−2101.
(25) Traub, M. C.; Longsine, W.; Truskett, V. N. Advances in Nanoimprint Lithography. *Annu. Rev. Chem. Biomol. Eng.* **2016**, *7*, 583−604.
(26) Guo, L. J. Nanoimprint Lithography: Methods and Material Requirements. *Adv. Mater.* **2007**, *19*, 495−513.
(27) Pirani, F.; Sharma, N.; Moreno-Cencerrado, A.; Fossati, S.; Petri, C.; Descrovi, E.; Toca-Herrera, J. L.; Jonas, U.; Dostalek, J. Optical Waveguide-Enhanced Diffraction for Observation of Responsive Hydrogel Nanostructures. *Macromol. Chem. Phys.* **2017**, *218*, No. 1600400.
(28) Mourran, A.; Zhang, H.; Vinokur, R.; Möller, M. Soft Microrobots Employing Nonequilibrium Actuation Via Plasmonic Heating. *Adv. Mater.* **2017**, *29*, No. 1604825.
(29) Volk, K.; Fitzgerald, J. P. S.; Retsch, M.; Karg, M. Time-Controlled Colloidal Superstructures: Long-Range Plasmon Resonance Coupling in Particle Monolayers. *Adv. Mater.* **2015**, *27*, 7332.
(30) Valsecchi, C.; Brolo, A. G. Periodic Metallic Nanostructures as Plasmonic Chemical Sensors. *Langmuir* **2013**, *29*, 5638−5649.
(31) Halas, N. J.; Lal, S.; Chang, W.-S.; Link, S.; Nordlander, P. Plasmons in Strongly Coupled Metallic Nanostructures. *Chem. Rev.* **2011**, *111*, 3913−3961.
(32) Baffou, G.; Quidant, R. Thermo-Plasmonics: Using Metallic Nanostructures as Nano-Sources of Heat. *Laser Photonics Rev.* **2013**, *7*, 171−187.
(33) Brongersma, M. L.; Halas, N. J.; Nordlander, P. Plasmon-Induced Hot Carrier Science and Technology. *Nat. Nanotechnol.* **2015**, *10*, 25.
(34) Mayer, K. M.; Hafner, J. H. Localized Surface Plasmon Resonance Sensors. *Chem. Rev.* **2011**, *111*, 3828−3857.
(35) Goerlitzer, E. S. A.; Speichermann, L. E.; Mirzaa, T. A.; Mohammadia, R.; Vogel, N. Addressing the Plasmonic Hotspot Region by Site-Specific Functionalization of Nanostructures. *Nanoscale Adv.* **2020**, *2*, 136.
(36) Piliarik, M.; Kvasnicka, P.; Galler, N.; Krenn, J. R.; Homola, J. Local Refractive Index Sensitivity of Plasmonic Nanoparticles. *Opt. Express* **2011**, *19*, 9213−9220.
(37) Jonsson, M. P.; Dahlin, A. B.; Feuz, L.; Petronis, S.; Hook, F. Locally Functionalized Short-Range Ordered Nanoplasmonic Pores for Bioanalytical Sensing. *Anal. Chem.* **2010**, *82*, 2087−2094.
(38) Herzog, N.; Kind, J.; Hess, C.; Andrieu-Brunsen, A. Surface Plasmon & Visible Light for Polymer Functionalization of Mesopores and Manipulation of Ionic Permselectivity. *Chem. Commun.* **2015**, *51*, 11697−11700.
(39) Dostert, K.-H.; Álvarez, M.; Koynov, K.; del Campo, An.; Butt, H.-J. r.; Kreiter, M. Near Field Guided Chemical Nanopatterning. *Langmuir* **2012**, *28*, 3699−3703.
(40) Mazzotta, F.; Johnson, T. W.; Dahlin, A. B.; Shaver, J.; Oh, S. H.; Hook, F. Influence of the Evanescent Field Decay Length on the Sensitivity of Plasmonic Nanodisks and Nanoholes. *ACS Photonics* **2015**, *2*, 256−262.
(41) Wang, Y.; Brunsen, A.; Jonas, U.; Dostalek, J.; Knoll, W. Prostate Specific Antigen Biosensor Based on Long Range Surface Plasmon-Enhanced Fluorescence Spectroscopy and Dextran Hydrogel Binding Matrix. *Anal. Chem.* **2009**, *81*, 9625−9632.
(42) Huang, C. J.; Dostalek, J.; Knoll, W. Long Range Surface Plasmon and Hydrogel Optical Waveguide Field-Enhanced Fluorescence Biosensor with 3d Hydrogel Binding Matrix: On the Role of Diffusion Mass Transfer. *Biosens. Bioelectron.* **2010**, *26*, 1425−1431.
(43) Beines, P. W.; Klosterkamp, I.; Menges, B.; Jonas, U.; Knoll, W. Responsive Thin Hydrogel Layers from Photo-Cross-Linkable Poly (N-Isopropylacrylamide) Terpolymers. *Langmuir* **2007**, *23*, 2231−2238.
(44) Sergelen, K.; Petri, C.; Jonas, U.; Dostalek, J. Free-Standing Hydrogel-Particle Composite Membrane with Dynamically Controlled Permeability. *Biointerphases* **2017**, *12*, No. 051002.
(45) Gee, K. R.; Archer, E. A.; Kang, H. C. 4-Sulfotetrafluorophenyl (Stp) Esters: New Water-Soluble Amine-Reactive Reagents for Labeling Biomolecules. *Tetrahedron Lett.* **1999**, *40*, 1471−1474.
(46) Quilis, N. G.; Lequeux, M.; Venugopalan, P.; Khan, I.; Knoll, W.; Boujday, S.; de la Chapelle, M. L.; Dostalek, J. Tunable Laser Interference Lithography Preparation of Plasmonic Nanoparticle Arrays Tailored for Sers. *Nanoscale* **2018**, *10*, 10268.
(47) Dostalek, J.; Knoll, W.; Fossati, S.; Hageneder, S.; Jungbluth, V. Plasmon-Enhanced Fluorescence Spectroscopy Imaging by Multi-Resonant Nanostructures. European Patent Application No. 19164960.72019.
(48) Sharma, N.; Petri, C.; Jonas, U.; Dostalek, J. Reversibly Tunable Plasmonic Bandgap by Responsive Hydrogel Grating. *Opt. Express* **2016**, *24*, 2457−2465.
(49) Aulasevich, A.; Roskamp, R. F.; Jonas, U.; Menges, B.; Dostálek, J.; Knoll, W. Optical Waveguide Spectroscopy for the Investigation of Protein-Functionalized Hydrogel Films. *Macromol. Rapid Commun.* **2009**, *30*, 872−877.
(50) Bauch, M.; Toma, K.; Toma, M.; Zhang, Q.; Dostalek, J. Plasmon-Enhanced Fluorescence Biosensors: A Review. *Plasmonics* **2014**, *9*, 781−799.

https://dx.doi.org/10.1021/acs.jpcc.9b11059
J. Phys. Chem. C 2020, 124, 3297−3305